NUCL SCI TECH (2020) 31:110
https://doi.org/10.1007/s41365-020-00817-3

Design of a 162.5 MHz continuous-wave normal-conducting radiofrequency electron gun

Cheng Wang[1,2] · Zi-Han Zhu[1,2] · Zeng-Gong Jiang[3] · Qi-Sheng Tang[3] · Zhen-Tang Zhao[3] · Qiang Gu[3]

Received: 3 July 2020 / Revised: 12 October 2020 / Accepted: 13 October 2020 / Published online: 9 November 2020

Abstract A high-gradient radiofrequency (RF) gun operated in continuous-wave (CW) mode is required in various accelerating applications. Due to the high RF power loss, a traditional normal-conducting (NC) RF electron gun has difficulty meeting the requirement of generating a high-repetition-rate electron beam. The development of a scheme for a CW NC-RF gun is urgently required. Demonstrated as a photoinjector of a high-repetition-rate free-electron laser (FEL), an electron gun operated in CW mode and the VHF band is designed. An analysis of the reentrant gun cavity is presented in this paper to increase the gradient and decrease the power density and power dissipation. Referring to the analysis results, the design of a 162.5 MHz gun cavity is optimized by a multi-objective evolutionary algorithm to achieve better performance in CW mode. Multipacting and thermal analyses are also deliberated in the design to coordinate with RF and mechanical design. The optimized 162.5 MHz gun cavity can be operated in CW mode to generate a high-repetition-rate beam with voltage up to 1 MV and gradient up to 32.75 MV/m at the cathode.

Keywords High-repetition-rate beam · Radiofrequency gun · Continuous-wave mode · Multi-objective evolutionary algorithm

1 Introduction

A continuous-wave (CW) electron gun is conventionally applied in a high-repetition-rate X-ray free-electron laser (XFEL) to research atoms, molecules, and protein micro-crystals, and to solve further problems in materials, biology, chemistry, and energy science [1–3]. Traditional high-gradient normal-conducting (NC) radiofrequency (RF) photocathode electron guns are operated in pulsed mode, with a pulse time of several microseconds and a low duty factor of 0.024%–5% [4, 5], determined by facility requirements [6–13]. In addition, traditional photocathode guns operate at a frequency of 1–10 GHz, generating microwave-level peak power dissipation. The temperature of a traditional NC-RF photocathode electron gun falls between RF pulses. However, it has difficulty meeting the requirement of continuously generating a high-repetition-rate beam up to 1 MHz. Guns operated at a much higher duty factor are taken into consideration. When the duty factor is equal to one, the electron gun will work in CW mode, in which case it produces an electron beam without macropulse limitation.

Several types of electron gun are operated in CW mode, such as direct-current (DC) guns and very few NC-RF guns. First, the DC gun can be operated in CW mode to generate beams ranging from DC to any repetition rate. However, at present the gradient of a DC gun [14] makes it difficult to enhance brightness [15, 16]. In addition, special NC-RF designs that can be operated in CW mode can

✉ Qiang Gu
guqiang@sinap.ac.cn

1 Shanghai Institute of Applied Physics, Chinese Academy of Sciences, Shanghai 201800, China

2 University of Chinese Academy of Sciences, Beijing 100049, China

3 Shanghai Advanced Research Institute, Chinese Academy of Sciences, Shanghai 201210, China

achieve high gradient and high average brightness; for example, the 187 MHz gun from the Lawrence Berkeley National Laboratory (LBNL) [17]. However, it is challenging to obtain a higher gradient and lower heat load design. Moreover, a high-quantum-efficiency and long-lifetime photocathode is required. Comparing all these technologies, the very-high-frequency (VHF)-band gun based on the Advanced Photo-injector EXperiment (APEX) from LBNL has been finalized by compromising between the accelerating technologies, photocathode technologies, and cost. To date, the VHF gun has been applied in Linac Coherent Light Source (LCLS)-II [18] and researched at LBNL [19], Deutsches Elektronen-SYnchrotron (DESY) [20], and SHINE [21–23]. The work in this paper on the VHF-band gun will be a reference for optimizing RF designs with a multi-objective evolutionary algorithm (MOEA) approach.

The VHF-band gun works at a relatively low frequency, with a mechanically stable reentrant cavity of length almost $\lambda/4$, where λ is the wavelength of the eigenmode. The lower frequency leads to a larger cavity and longer wavelength. The reentrant shape can generate a higher electric field with the same power, and the larger cavity leads to lower surface power density and an easy-to-cool design. The long wavelength corresponds to a long beam length. A 30-ps-long electron beam occupies only 1.76° at 162.5 MHz. Hence, the beam can basically feel the same accelerating field and share the same physical process as a DC gun [24]. Meanwhile, the cutoff holes of a long-wavelength cavity can be larger, which is convenient for the detailed design of the cavity.

However, the high power dissipation of a CW gun is a major suppressing factor in the RF performance of the cavity. The power dissipation makes it difficult to increase the accelerating gradient on the cathode and output beam energy. Hence, the gun requires careful thermal design. Optimization of RF properties, thermal performance, and mechanical features is a good solution to guarantee stable performance of the gun. Typical optimization methods in RF design, such as scanning, are time-consuming processes. As the number of variables increases, the computation time increases exponentially. In this paper, we introduce an MOEA in the gun cavity RF design [25] to explore a better CW gun performance.

The design of a 162.5 MHz electron gun in this paper focuses on achieving an extremely high gradient with acceptable power loss and power density under a gap voltage higher than the APEX gun gap voltage of 750 kV. In Sect. 2, the overall RF design of the gun is described. An analysis of the geometric parameters of the main RF properties is presented and used as a reference for optimization. Subsequently, the optimization based on an MOEA is presented. The optimal solutions provide cavities under extreme conditions. In Sect. 3, a numerical simulation of multipacting in the cavity and the scheme of suppression is presented. In Sect. 4, a simulation of the temperature and deformation distribution is presented. Finally, a systemic gun design with good RF and mechanical performance is obtained.

2 RF design of the electron gun

One of the most significant tasks in the RF design of the VHF gun is obtaining the detailed structure of the electron gun cavity. The ideal design involves a high accelerating gradient to preserve the beam brightness by reducing the space-charge effects for relatively low-energy electron beams, low power dissipation to reduce thermal stress, and low peak electric field intensity to reduce the possibility of breakdown during operation. The gun cavity will be analyzed by scanning the main geometry size at first, and the results will serve as references for optimization.

2.1 Cavity analysis

The VHF gun cavity RF design starts from the half-reentrant cavity in Fig. 1, which includes a small reentrant anode. The anode will help to increase the shunt impedance. Therefore, the power dissipation and power density can be lowered.

For free-electron laser (FEL) operation, the frequency of the gun cell should be chosen as a subharmonic of the main frequency 1.3 GHz, making the gun operation compatible with the Teraelectronvolt Energy Superconducting Linear Accelerator (TESLA). Figure 2 shows a preliminary comparison between the scaled 144, 162.5, 185.7, and 216.6 MHz cavities. In Fig. 2a, the power density along the cavity surface at a gap voltage of 750 kV is presented. A higher power density appears at the cathode and anode nose cone, and the peak power density appears near the cathode.

At lower frequencies, the power density on the cavity walls will be reduced. At 750 kV, the peak power density of the 216.6 MHz cavity is more than 28 W/cm^2, and the peak power density of the 162.5 MHz one is 15.2 W/cm^2. Operating at a lower frequency benefits the thermal design and voltage-boosting operation. Although the shunt impedance per unit length is lower, the electric field at the cathode will still be increased with a higher gap voltage, which also benefits the beam quality. However, as shown in Fig. 2b, the 144.4 MHz cavity appears much larger than the processing capacity of 41 cm. Therefore, the 162.5 MHz cavity is now selected as the baseline of the electron gun.

Fig. 1 Geometry and schematics of reentrant-anode VHF gun cavity

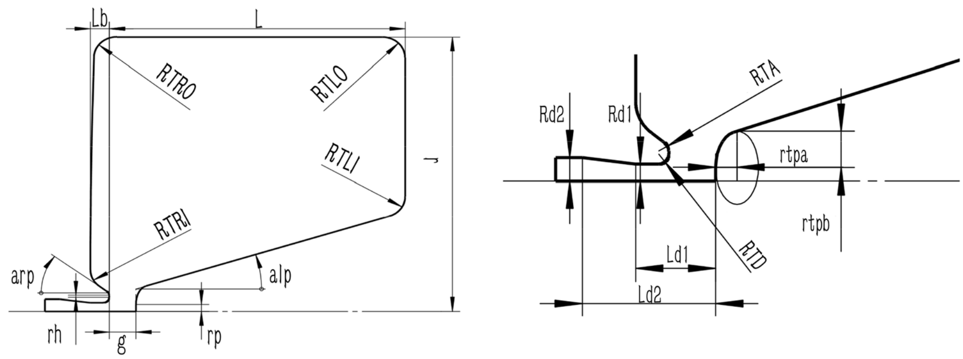

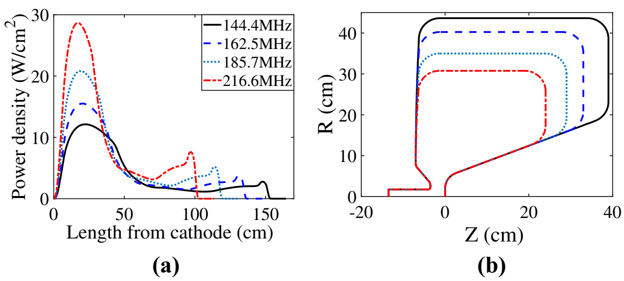

Fig. 2 (Color online) Comparison of cavities at different frequencies. Power density along the cavity wall (**a**) and the cross section comparison of the cavities (**b**)

The RF parameters of the cavity of the electron gun can be optimized by adjusting the geometry. Determination of the main parameter of the nose cone finalizes the capacitance, so that the acceleration field distribution can only be optimized by structures near the gap, and the RF properties, such as the Q factor, power dissipation, and power density, are mainly optimized by the adjustment of other external dimensions.

By scanning the structural size of the electron gun cavity, which is described by 19 independent geometric parameters in Fig. 1, RF parameters including the power loss (P), maximum surface power density (MaxPd) , maximum surface electric field (MaxE), on-axis electric field on the cathode (Ezc), stored energy (W), and impedance considering the transit time factor (ZTT) are announced. In the LRC circuit of the cavity, some RF parameters can be described by the expressions

$$P = \frac{V_c^2}{2R}, W = \frac{CV_c^2}{2}, \omega = \frac{1}{\sqrt{LC}}, \quad (1)$$

where V_c and ω are the voltage and circular frequency of the cavity, respectively. Because the voltage and frequency remain constant during the scanning, the change in power loss (P) can be attributed to the change in impedance (R), and the change in stored energy (W) can be attributed to the change in capacitance (C).

The accelerating gap is the most important geometric parameter in the gun cavity because the distribution of the axial electric field is determined dominantly by the gap g. The RF properties and electric field along the beam line from SUPERFISH are shown in Fig. 3. As shown, a long accelerating gap helps to control the maximum electric field and maximum power density, while a short acceleration gap is beneficial for increasing the electric field on the cathode (Ezc). When the gap is too small, the capacitance increases and the inductance decreases. The required RF power increases rapidly owing to the smaller impedance. However, when the gap is too large, the transit time factor will decrease. For a compromise between high shunt impedance and high cathode field under a defined gun voltage, the accelerating gap is set as 3.5 cm.

For the remaining geometric sizes, with the cathode nose cone angle (alp) varying, the power loss (P), and peak power density (MaxPd) change differently. As shown in Fig. 4a, as the power loss (P) and stored energy (W) increase, the peak power density decreases significantly. With respect to cavity length (L), the stored energy (W) first decreases and then increases, whereas the peak power density only increases (Fig. 4b). The peak electric field (Max$E$) and the electric field on the cathode (Ezc) are more sensitive to the horizontal (rtpa) and vertical (rtpb) dimensions of the cathode cone blend compared to the nose angle (alp) and cavity length (L).

The results in Fig. 5 show the dependence of the RF properties on the dimensions of the anode structure.

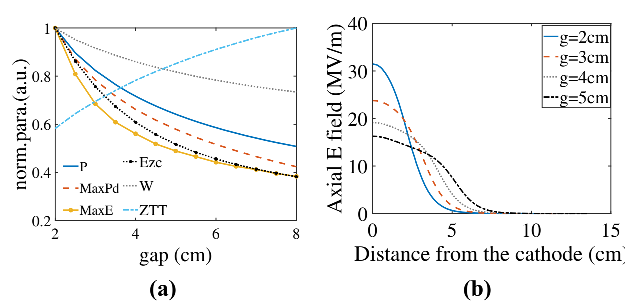

Fig. 3 (Color online) RF properties trend from scanning the accelerating gap size using SUPERFISH [26] (**a**). Field distribution of different gap sizes (**b**)

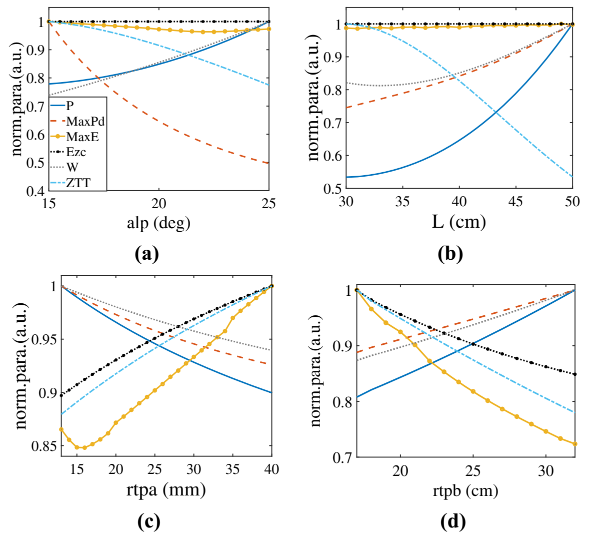

Fig. 4 (Color online) RF properties from scanning the cathode-side structural size: nose cone angle (**a**), cavity length (**b**), horizontal dimension of the nose cone ellipse (**c**), vertical dimension of the nose cone ellipse (**d**), using SUPERFISH

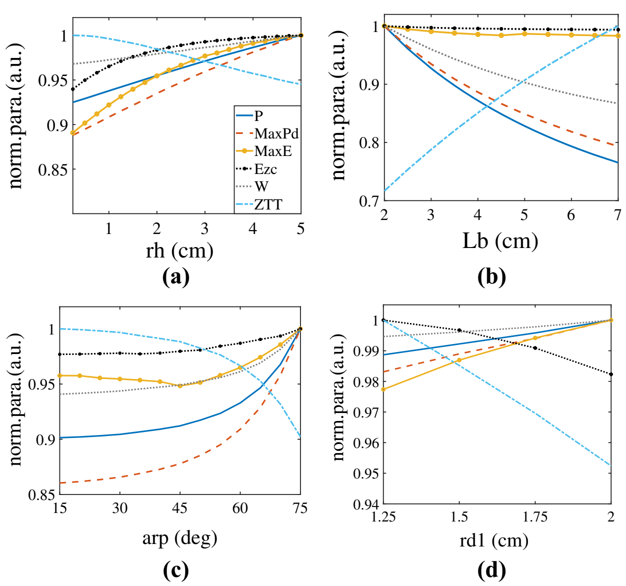

Fig. 5 (Color online) RF properties from scanning the anode-side structural size: anode cone size (**a**), anode length (**b**), elevation angle (**c**), beam pipe radius (**d**), using SUPERFISH

Increasing the length of the anode (lb) in the scanning range can decrease the power dissipation and power density. The anode cone size (rh) and beampipe radius (rd1) should be lowered to obtain lower power dissipation (*P*) and power density (MaxPd). In addition, the reduction of the beampipe radius (rd1) also increases the E-field at the cathode. A minimum value of maximum surface electric field (MaxE) occurs with increasing elevation angle (arp).

2.2 Gun cavity optimization

The analysis above illustrates how the geometric parameters influence the RF properties and determine the value range of each variable. These geometric parameters must be optimized to increase the electric field at the cathode and decrease the power loss in the selected frequency. The maximum power density, peak electric field, and cavity size are also considered in this optimization. Scanning is a common method of optimization with running time constraints. In addition, based on the weighted method, the single-objective evolutionary algorithm is widely used for the optimization problem with multiple objectives; however, the weights are difficult to determine, and the opportunity to analyze the relationship between different objectives could therefore be lost. Here, an MOEA is employed to solve this problem.

The MOEA approach was first used in photoinjector design in 2005 [27] and has been applied in many aspects of accelerator science [28]. This type of algorithm is a method of searching for the optimal solution by simulating natural evolution. In this task, the non-dominated sorting genetic algorithm II (NSGA-II) [29] is used as the optimizer and SUPERFISH is used as the operator. Typical genetic algorithms include selection, crossover, and mutation operators. The selection operator determines the strategy of the selected population to be inherited by the next generation from the former one. The crossover operator is used to generate a new individual under a specific method. The mutation operator imitates the mutation process in biological genetics and evolution, which is a relatively low possibility but non-negligible way to generate new individuals.

The main optimization objective of the electron gun cavity is a high electric field at the cathode, which leads to low emittance and high brightness. The power loss is expected to be as low as possible. The following constraints are added to the optimizations: The well-known Kilpatrick criterion scaling [30] can be applied to calculate the breakdown threshold field. The operating peak electric field in the CW cavity can be up to 2 kilp (two times the Kilpatrick criterion value); however, it is possible to enhance a higher peak surface field with present technology. Therefore, the designed limitation of the peak surface electric field is 3 kilp, which is up to 40 MV/m at 162.5 MHz under a voltage of 1 MV. The power density, which has a strong correlation with power loss, should be lowered. An acceptable surface power density is 35 W/cm^2 with present cooling technology. Although the solenoid of the injector is designed to be downstream of the gun, a magnetic field that can affect beam quality may still exist. A small solenoid with opposite current is placed beyond the cathode to cancel the magnetic field on the cathode. To ensure sufficient space in the nose cone, the cathode plate should not be too small. Therefore, rp should be moderate in size. In addition, lb and l are limited by multipacting considerations as the radius is limited by the manufacturing process.

The main limitations and parameter range discussed above are summarized in Table 1.

A two-objective optimization for gun cavity design, including the E-field on the cathode and power loss from the SUPERFISH solution, is performed. The result of the optimization of the 162.5 MHz cavity is presented in Fig. 6. To optimize more objectives, a three-objective optimization with peak E-field serving as an objective instead of a limitation in the algorithm is also shown (Fig. 7). The red points in Fig. 7 denote data sets with maximum electric field less than 2.25 kilp and power loss less than 67.5 kW under 750 kV voltage.

The process is repeated several times to verify the results. For a population of 120, at the 50th generation, good convergence is achieved in the two-objective optimization in the targeted objective range. The Pareto front shows the trade-off between the high cathode *E*-field and low power loss. Therefore, the conclusion can be drawn that a mutually exclusive relationship exists between the gradient on the cathode and power loss. The three-objective optimization is discussed at the 75th generation. A strong positive correlation exists between the maximum *E*-field and the *E*-field at the cathode. However, the positive relationship and the trade-off between maximum *E* and power loss influence the balance between *E* at the cathode and power loss. Hence, the best solution in the three-objective optimization is the point with the lowest power loss and the highest *Ezc*. Nevertheless, the optimal solutions in the two-objective optimization perform better with lower power loss, whereas *Ezc* and Max*E* are almost the same for the best solution of the three-objective optimization. Therefore, the working point is depicted in Fig. 7. The RF properties at the selected working point are presented in Table 2 (Cavity (optimized)).

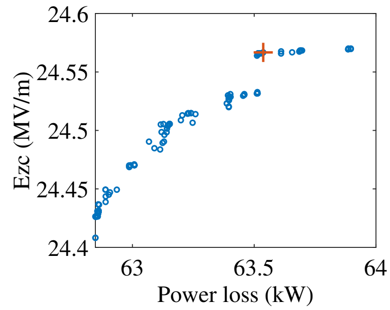

Fig. 6 (Color online) Optimal solution of power dissipation and E-field at the cathode from the 162.5 MHz cavity with a population size of 120 in the 50th generation. The red + denotes the selected working point

Compared with the unoptimized 162.5 MHz arc-anode cavity presented in Table 2 (Cavity (w/o optimization)), the electric field at the cathode increases to 24.57 MV/m from 21 MV/m, and the power loss decreases to 63.5 kW from 78 kW. Under a 1 MV state, the electric field on the cathode will be 32.76 MV/m, with 112.9 kW power dissipation and 32.1 W/cm^2 peak power density. The 2D geometry overlap display comparison is also presented in Fig. 8. Compared with the 162.5 MHz APEX2 gun cell, the peak power density of the optimized cavity in this study will be lower at 820 kV. The gradient at the cathode of the APEX2 gun cell is higher because of the smaller gap. In this study, the number of objectives is no more than three. In subsequent research, NSGA-III [31] will be developed to continue the optimization by exploring the interconnection between four or more objectives.

2.3 Coupler RF design

For the frequency of 162.5 MHz in the gun cavity design above, the waveguide size will be close to 95 cm × 50 cm if the RF power is transmitted through a rectangular waveguide. Thus, the coupler is designed as a dual coaxial loop coupler to cancel the dipole mode in the cavity and decrease the feed power in each coupler.

Table 1 Limitations in optimization

Objective	Limitation		Goal
Frequency, *f*	162.5 MHz		Maximize Ezc
Radius, *r*	≤ 400 mm		
Length, *L*	350–400 mm		
Gap, *g*	≥ 30 mm		
Cathode, rp	≥ 20 mm		
Voltage	750 kV	1 MV	Minimize power loss
MaxE	≤ 2.25 kilp	≤ 3 kilp	
MaxPd	≤ 19.68 W/cm^2	≤ 35 W/cm^2	

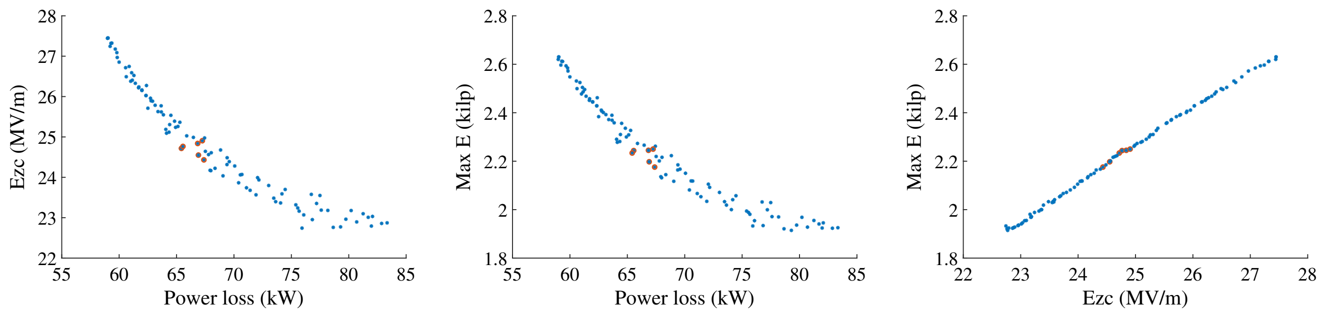

Fig. 7 (Color online) Projections of the optimal solution of three objectives. Red points are selectable cases

Table 2 RF properties of each cavity

Type	APEX	APEX2 (gun cell)	Cavity (w/o optimization)	Cavity (optimized)
Frequency (MHz)	186	162.5	162.5	162.5
Voltage (kV)	750	820	750	750
R (cm)	34.7	39.5	38.8	39.9
Gap (cm)	4	2.5	3.5	3.5
Power dissipation (kW)	87.5	90.7	78.61	63.512
Max power density (W/cm^2)	25	32.1	15.569	18.05
E at cathode (MV/m)	19.47	34	21.01	24.57
Max E (MV/m)	24.1	37	26.02	30.61

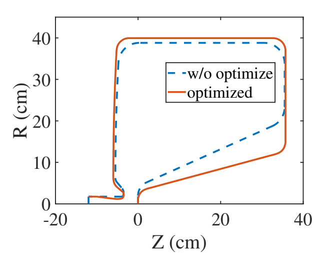

Fig. 8 (Color online) Sectional geometry comparison between the optimized cavity and the cavity without optimization

Under a 162.5 MHz, 1 MV state, the power dissipation of the cavity is optimized to be less than 120 kW. The power that a single coupler must transmit is up to 60 kW. According to Electronic Industry Alliance (EIA) standards, both a 4-1/16- and 6-1/8-inch coaxial waveguide can meet the requirements [32]. However, the compact backboard area of the cavity suggests that it is better for the 4-1/16-inch coaxial waveguide to be applied to connect with two symmetrically placed magnetic coupling antennas (Fig. 9).

The required coupling coefficient β_0 can be calculated with the given beam parameter:

$$\beta_{\text{loaded}} = \frac{P_{\text{external}}}{P_{\text{total}}} = \frac{P_{\text{external}}}{P_{\text{cavity}} + P_{\text{beam}}}, \tag{2}$$

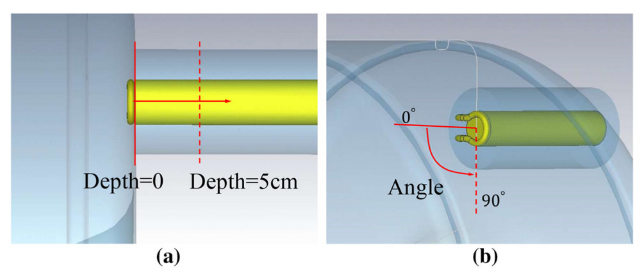

Fig. 9 (Color online) Coupler design in CST [33]. The movement direction of coupling depth (**a**), and the rotation angle of coupler loop from 0° to 90° (**b**)

$$\beta_0 = \frac{P_{\text{external}}}{P_{\text{cavity}}}. \tag{3}$$

It is required that the coupler does not reflect power when operating with a beam load ($\beta_{\text{loaded}} = 1$).

$$\beta_0 = \frac{P_{\text{cavity}} + P_{\text{beam}}}{P_{\text{cavity}}}. \tag{4}$$

The designed P_{beam} is very low; thus, β_0 is required to be close to 1 [34]. For another description of the coupling coefficient of loop coupling in an LCR equivalent circuit [35–37],

$$\beta_0 = \frac{(\omega_0 \mu_0 A \cos\theta)^2}{2} \frac{Z_W}{Z_W{}^2 + (\omega L_L)^2} \frac{H_1{}^2}{P_{cavity}}, \tag{5}$$

where Z_W is the characteristic impedance of the transmission line, H_1 is the peak magnetic field on the loop, L_L is the self-inductance of the coupler loop, A is the area of the antenna, and θ is the angle between the antenna and the magnetic field. The coupling coefficient can be adjusted by the depth and angle of the antenna entering the cavity. During actual assembly and commissioning, the positions of the coupler and cavity are fixed, and the coupler antenna is rotated to accurately obtain the correct coupling.

The coupling coefficient and quality factor vary with the depth and angle of the antenna, as shown in Fig. 10. Owing to the installation of the coupler, the frequency of the cavity will slightly shift from 162.498 to 162.32 MHz. When the angle turns to near 0°, the coupling is very weak, and the result might be inaccurate. To adjust the coupling coefficient more accurately, the coupling loops are designed to be approximately 45° when achieving the best coupling.

3 Multipacting study

In CW mode, multipacting is an important element to be considered. Multipacting is a phenomenon in which electrons are emitted from the surface of the cavity, driven by the field, and impact the cavity wall [38]. This happens in certain resonant conditions such as a weak-electric-field area in which the magnetic field is relatively strong [39]. When multipacting starts, more secondary electrons are released and accelerated by the field. The number of total electrons then increases exponentially. This process can consume power in the cavity, cause breakdown, and possibly damage or even destroy the high-power RF device. The CST Particle Studio tracking module is applied for 3D multipacting tracking simulation, with the second-emission-yield (SEY) curve of annealed copper given in CST. The growth rate is calculated by fitting $N(t) = N_0 e^{\alpha t}$, where N_0 is the number of initial particles and α is the growth rate. Multipacting, which is a first-order single point, starts at the cavity wall, near the anode side (Fig. 11).

Because the number of secondary electrons is strongly dependent on the impact energy and surface material, surface treatment is a possible solution. However, for simulation, the general and fundamental solution is to avoid the resonant condition by geometry optimization.

As shown in Fig. 12, by adding wrinkles to the cavity wall, multipacting is controlled effectively. The RF properties of the modified cavity hardly change. Particle growth is limited to a small range at the lower-voltage end. At higher voltages, the resonance conditions are not met; hence, the gun cavity can be operated in a field between 750 kV and 1 MV without multipacting.

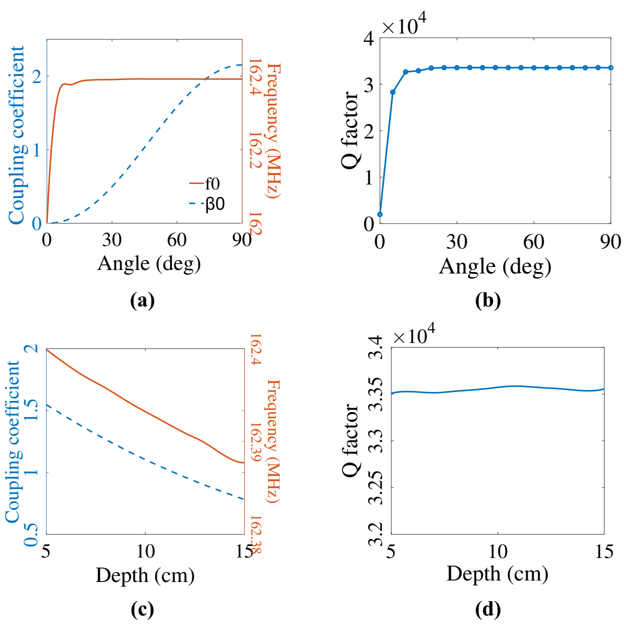

Fig. 10 (Color online) Coupling parameters varying with coupler angle at a depth of 11 cm (**a**, **b**), and coupling depth at an angle of 45° (**c**, **d**)

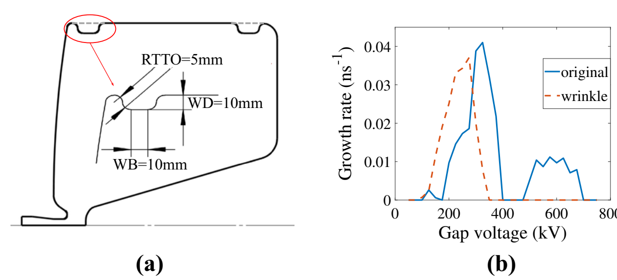

Fig. 12 (Color online) Model of the cavity with wrinkles (**a**) and multipacting region of different cavities (**b**); the wrinkled cavity will experience a high-power RF condition at 120–360 kV to overcome the multipacting zone

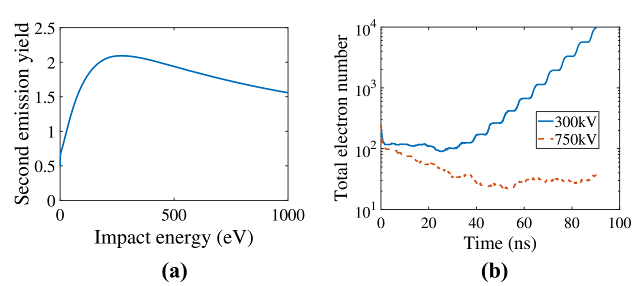

Fig. 11 (Color online) SEY curve used in the multipacting study (**a**), and particle growth simulated by the CST Particle Studio tracking module (**b**)

4 Thermal and structural analysis

Because the 162.5 MHz NC-RF gun is operated in CW mode, the gun cavity will be heated and thermally deformed, resulting in a detuning in frequency, which should be considered simultaneously with cavity design and tuning. To reduce thermal stress and material fatigue, it is necessary to cool the gun to an appropriate temperature. Under the considerations above, the stress and deformation of the electron gun under the combined actions of heat, cooling, support constraints, vacuum pressure, and gravity are analyzed.

A cross section of the gun is shown in Fig. 13. The cavity is nested in a vacuum steel sleeve and pumped through the slot on the cavity wall to ensure a vacuum in the cavity. The cooling circuit is distributed around the cavity, as a jacket with two spiral cooling circuits welded to the cathode nose cone. The heat load on the cavity wall can be removed by convection heat exchange between the cooling water and the wall. The design of the cooling loops requires sufficient water to reduce the temperature rise of the cooling water, to prevent the cooling water from boiling under the working water pressure. The cooling loops should be placed according to the distribution of power density to minimize the maximum temperature of the cavity.

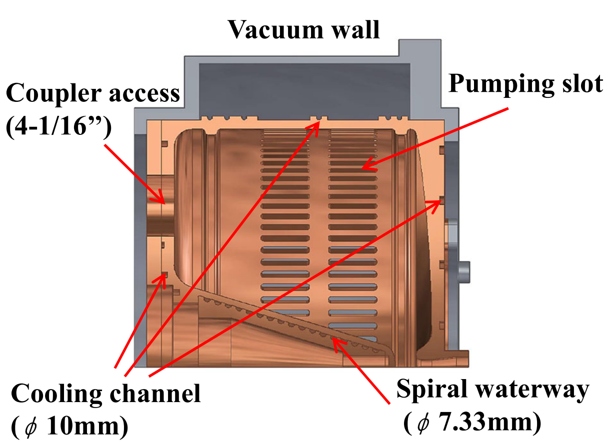

Fig. 13 (Color online) Mechanical 3D model of the VHF electron gun

Under full-power operation, the total heat load on the cavity is 113 kW, of which approximately 19.4 kW is on the outer cylinder cavity wall, 10.55 kW on the anode-side wall surface, 22.8 kW on the end plate wall surface, and 46.94 kW on the cathode cone. Empirical formulas for convective heat transfer coefficients are used in the simulation in ANSYS [40] and the CST Multiphysics module to determine the cavity temperatures and deformation in steady state. The diameter of the cooling channel is 8 mm around the outer cavity wall, and 7.33 mm around the cathode nose. The heat transfer coefficient (HT coeff) set in the simulation is calculated from the design features in Table 3.

The temperature simulation in the state of 1 MV, with 113 kW power and 26 °C initial temperature, is presented in Fig. 14. The hottest area reaches a temperature of 61.6 °C. It appears at the transitional arc area of the cathode cone and the cathode plate, located near the highest power density. This is because the small-degree cone is far from the cooling channel. The temperature at the cathode nose cone is approximately 53.4 °C, and that at the anode nose cone is approximately 46 °C. Under the state of 63.512 kW, 750 kV, the highest temperature is 50 °C. The temperature at the cathode nose cone is approximately 46 °C, and that at the anode nose cone is approximately 39 °C.

To obtain the deformation and stress distribution, the temperature distribution obtained by simulation under full power is loaded with the boundary conditions shown in Fig. 15a. The cutting planes (A,B) and a plane of the steel sleeve are set as the displacement, and the atmospheric pressure and gravity are also considered. The maximum deformation of the electron gun is 0.22 mm, which occurs on the back plate of the stainless-steel sleeve, as shown in Fig. 16. As atmospheric pressure is applied to the cavity,

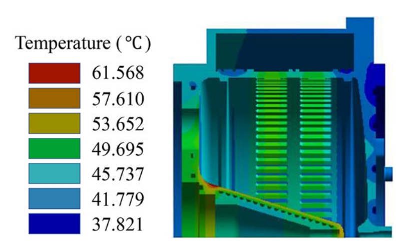

Fig. 14 (Color online) Temperature distribution of the cavity under full power

Table 3 Cooling parameters set in the simulation

Position	Outer wall	Anode	Back end	Cathode nose
Channel diameter (mm)	8	10.2	10	7.33
Flow velocity (m/s)	4.3	1.8	2.4	6.4
HT coeff (W/m^2 K)	17,996	8364	10,638	24,715

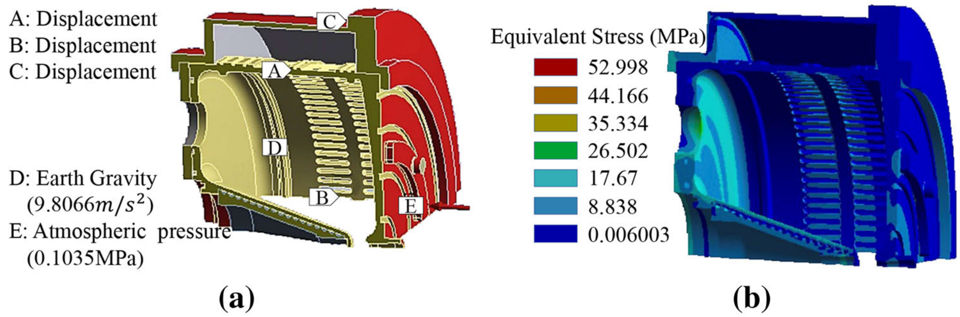

Fig. 15 (Color online) Boundary condition for the deformation simulation (**a**) and the distribution of stress (**b**) inside the cavity under full power (1 MV). The maximum stress of 53 MPa occurs at the contact between the back end of the cavity nose and the cooling plug

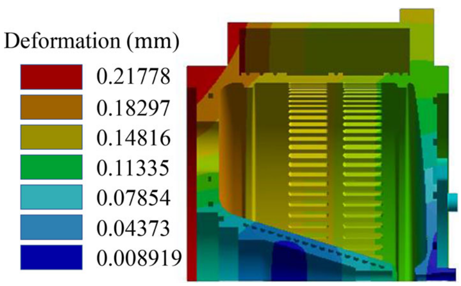

Fig. 16 (Color online) Deformation of the cavity under full power

the cathode and anode noses deform closer to each other by approximately 0.06 mm. The total deformation caused by the temperature increase corresponds to a cavity frequency shift of approximately 0.2 MHz from 162.303 to 162.499 MHz under full power. With the water-cooled channels coiled around the cavity, the heat load and thermal stresses are managed carefully. The frequency shift is tuned by a tuner on the anode plate. Hence, the electron gun cavity can work stably at the designed full voltage.

5 Conclusion

In this study, a CW NC-RF electron gun is designed systemically. An MOEA is introduced into the design to optimize the RF performance. The results suggest that the optimized 162.5 MHz gun cavity can achieve a gradient of up to 32.75 MV/m when reducing the heat load on the gun cavity to 113 kW. In this state, the output beam energy is 1 MeV. Theoretically, the emittance will be lower with a higher gap voltage and higher gradient on the cathode.

The CW VHF-band photoinjector is an effective solution for improving both average brightness and peak brightness in an XFEL. In subsequent research, a 162.5 MHz CW NC-RF gun will be developed using further mechanical design and fabrication processes. With further developments based on the electron gun in this study, such as multi-cell VHF gun and VHF self-resonant frequency gun design, more optimization goals are expected. More advanced optimization methods that can handle more objectives will be developed to deal with many-objective optimization problems (MaOP) and analyze the relationships between each objective. Moreover, the gun will be considered together with beam dynamics to obtain a low-emittance and high-quality injector.

References

1. M.P. Minitti, J.M. Budarz, A. Kirrander et al., Imaging molecular motion: femtosecond x-ray scattering of an electrocyclic chemical reaction. Phys. Rev. Lett. **114**, 255501 (2015). https://doi.org/10.1103/PhysRevLett.114.255501
2. C. Feng, H.X. Deng, Review of fully coherent free-electron lasers. Nucl. Sci. Tech. **29**, 160 (2018). https://doi.org/10.1007/s41365-018-0490-1
3. Z.T. Zhao, C. Feng, K.Q. Zhang, Two-stage EEHG for coherent hard X-ray generation based on a superconducting linac. Nucl. Sci. Tech. **28**, 117 (2017). https://doi.org/10.1007/s41365-017-0258-z
4. D.H. Dowell, E. Jongewaard, J. Lewandowski et al., The development of the linac coherent light source RF Gun. ICFA Beam Dyn. Newslett. **46**, 162–192 (2008)
5. R. Rimmer, N. Hartman, S. Lidia et al. High-gradient high-duty-factor rf photo-cathode electron gun. NASA STI/Recon Technical Report N
6. C.J. Tan, C.X. Tang, W.H. Huang et al., Beam and image experiment of beam deflection electron gun for distributed X-ray sources. Nucl. Sci. Tech. **30**, 50 (2019). https://doi.org/10.1007/s41365-019-0561-y
7. X. Li, J.Q. Zhang, G.Q. Lin et al., Performance of an electron linear accelerator for the first photoneutron source in China. Nucl. Sci. Tech. **30**, 53 (2019). https://doi.org/10.1007/s41365-019-0576-4
8. Z. Wang, C. Feng, Q. Gu et al., Generation of double pulses at the shanghai soft X-ray free electron laser facility. Nucl. Sci. Tech. **28**, 28 (2017). https://doi.org/10.1007/s41365-017-0188-9
9. H.P. Geng, J.H. Chen, Z.T. Zhao, Scheme for generating 1 nm X-ray beams carrying orbital angular momentum at the SXFEL. Nucl. Sci. Tech. **31**, 88 (2020). https://doi.org/10.1007/s41365-020-00794-7
10. Y.Y. Xia, Z.T. Zhao, Y.B. Zhao et al., Transfer function measurement for the SSRF SRF system. Nucl. Sci. Tech. **30**, 101 (2019). https://doi.org/10.1007/s41365-019-0612-4
11. C.H. Miao, M. Liu, C.X. Yin et al., Precise magnetic field control of the scanning magnets for the aptron beam delivery system. Nucl. Sci. Tech. **28**, 172 (2017). https://doi.org/10.1007/s41365-017-0324-6

12. B.C. Jiang, G.Q. Lin, B.L. Wang et al., Multi-bunch injection for SSRF storage ring. Nucl. Sci. Tech. **26**, 050101 (2015). https://doi.org/10.13538/j.1001-8042/nst.26.050101
13. T. Phimsen, B.C. Jiang, H.T. Hou et al., Improving Touschek lifetime and synchrotron frequency spread by passive harmonic cavity in the storage ring of SSRF. Nucl. Sci. Tech. **28**, 108 (2017). https://doi.org/10.1007/s41365-017-0259-y
14. B. Dunham, J. Barley, A. Bartnik et al., Record high-average current from a high-brightness photoinjector. Appl. Phys. Lett. **102**, 034105 (2013). https://doi.org/10.1063/1.4789395
15. I.V. Bazarov, B.M. Dunham, C.K. Sinclair, Maximum achievable beam brightness from photoinjectors. Phys. Rev. Lett. **102**, 104801 (2009). https://doi.org/10.1103/PhysRevLett.102.104801
16. D. Filippetto, P. Musumeci, M. Zolotorev et al., Maximum current density and beam brightness achievable by laser-driven electron sources. Phys. Rev. ST Accel. Beams **17**, 024201 (2014). https://doi.org/10.1103/PhysRevSTAB.17.024201
17. F. Sannibale, D. Filippetto, C. Papadopoulos et al., Advanced photoinjector experiment photogun commissioning results. Phys. Rev. Spec. Top. Accel. Beams **15**, 103501 (2012). https://doi.org/10.1103/PhysRevSTAB.15.103501
18. F. Zhou et al., in *Proceedings, 10th International Particle Accelerator Conference (IPAC2019): Melbourne, Australia*, 19–24 May, 2019, First Commissioning of LCLS-II CW Injector Source. 2019, p. TUPTS106. https://doi.org/10.18429/JACoW-IPAC2019-TUPTS106
19. T. Luo, H. Feng, D. Filippetto et al., RF design of APEX2 two-cell continuous-wave normal conducting photoelectron gun cavity based on multi-objective genetic algorithm. Nucl. Instrum. Methods Phys. Res. Sect. A Accel. Spectrom. Detect. Assoc. Equip. **940**, 12–18 (2019). https://doi.org/10.1016/j.nima.2019.05.079
20. G. Shu, Y. Chen, S. Lal et al., in *Proceedings, 10th International Particle Accelerator Conference (IPAC2019): Melbourne, Australia, 19–24 May*, 2019, first design studies of a NC CW RF gun for European XFEL. 2019, p. TUPRB010. https://doi.org/10.18429/JACoW-IPAC2019-TUPRB010
21. Z. Zhao, D. Wang, Z. Yang et al., in *Proceedings of International Free Electron Laser Conference (FEL'17), Santa Fe, NM, USA, August 20-25, 2017, SCLF: An 8-GeV CW SCRF Linac-Based X-Ray FEL Facility in Shanghai. No. 38 in International Free Electron Laser Conference (JACoW, Geneva, Switzerland, 2018)*, pp. 182–184. https://doi.org/10.18429/JACoW-FEL2017-MOP055
22. J. Yan, H. Deng, Multi-beam-energy operation for the continuous-wave X-ray free electron laser. Phys. Rev. Accel. Beams **22**, 090701 (2019). https://doi.org/10.1103/PhysRevAccelBeams.22.090701
23. Z. Wang, C. Feng, D.Z. Huang et al., Nonlinear energy chirp compensation with corrugated structures. Nucl. Sci. Tech. **29**, 175 (2018). https://doi.org/10.1007/s41365-018-0512-z
24. J. Schmerge, A. Brachmann, D. Dowell et al., in *The LCLS-II Injector Design*. Basel, Switzerland, 2014, pp. 815 – 819, accelerating gradient; Continuous waves; Design challenges; High repetition rate; Performance requirements; Repetition rate; Spectral range; Superconducting linear accelerators
25. M. Kranjčević, A. Adelmann, P. Arbenz et al., Multi-objective shape optimization of radio frequency cavities using an evolutionary algorithm. Nucl. Instrum. Methods Phys. Res. Sect. A Accel. Spectrom. Detect. Assoc. Equip. **920**, 106–114 (2019). https://doi.org/10.1016/j.nima.2018.12.066
26. K. Halbach, R.F. Holsinger, SUPERFISH - a computer program for evaluation of RF cavities with cylindrical symmetry. Part. Accel. **7**, 213–222 (1976)
27. I.V. Bazarov, C.K. Sinclair, Multivariate optimization of a high brightness DC gun photoinjector. Phys. Rev. Spec. Top. Accel. Beams **8**, 034202 (2005). https://doi.org/10.1103/PhysRevSTAB.8.034202
28. R. Bartolini, M. Apollonio, I. Martin, Multiobjective genetic algorithm optimization of the beam dynamics in linac drivers for free electron lasers. Phys. Rev. Spec. Top. Accel. Beams (2012). https://doi.org/10.1103/PhysRevSTAB.15.030701
29. K. Deb, A. Pratap, S. Agarwal et al., A fast and elitist multiobjective genetic algorithm: NSGA-II. IEEE Trans. Evol. Comput. **6**, 182–197 (2002). https://doi.org/10.1109/4235.996017
30. W. Kilpatrick, Criterion for vacuum sparking designed to include both RF and DC. Rev. Sci. Instrum. **28**, 824–826 (1957). https://doi.org/10.1063/1.1715731
31. J. Yan, H. Deng, Generation of large-bandwidth X-ray free electron laser with evolutionary many-objective optimization algorithm. Phys. Rev. Accel. Beams **22**, 020703 (2019). https://doi.org/10.1103/PhysRevAccelBeams.22.020703
32. Coax components specifications. https://www.shively.com/wp-content/uploads/2018/04/tb-linespecs.pdf
33. Cst studio suite, cst mircowave studio. https://www.3ds.com/products-services/simulia/products/cst-studio-suite/
34. K. Liu, L. Li, C. Wang et al., Multi-port cavity model and low-level RF systems design for VHF gun. Nucl. Sci. Tech. **31**, 8 (2020). https://doi.org/10.1007/s41365-019-0711-2
35. S. Lal, Study of the effect of loop inductance on the RF transmission line to cavity coupling coefficient. Rev. Sci. Instrum. **87**, 083308 (2016). https://doi.org/10.1063/1.4961578
36. Z.B. Li, A. Grudiev, W.C. Fang et al., Radio-frequency design of a new c-band variable power splitter. Nucl. Sci. Tech. **30**, 100 (2019). https://doi.org/10.1007/s41365-019-0611-5
37. Y. Liao, S. Wang, H. Guo et al., Design and implementation of wide range and high precision electron gun control system. Nucl. Tech. **42**, 020202 (2019). https://doi.org/10.11889/j.0253-3219.2019.hjs.42.020202 (in Chinese)
38. E. Somersalo, P. Yla-Oijala, D. Proch, in *Proceedings Particle Accelerator Conference, Analysis of Multipacting in Coaxial Lines*, vol. 3, pp. 1500–1502. IEEE (1995). https://doi.org/10.1109/PAC.1995.505264
39. Z. Yao, R. Laxdal, V. Zvyagintsev et al., in *Multipacting Suppression in a Single Spoke Cavity*. THP034, these proceedings
40. Ansys multiphysics. https://www.ansys.com/products/platform/multiphysicssimulation